AGU PUBLICATIONS

Geophysical Research Letters

Supporting Information for

Revisiting ENSO and IOD contributions to Australian Precipitation

Giovanni Liguori[1,2], Shayne McGregor[1], Martin Singh[1], Julie Arblaster[1,3], and Emanuele Di Lorenzo[4]

1. ARC Centre of Excellence for Climate Extremes, Monash University, Clayton, Australia
2. Department of Physics and Astronomy, University of Bologna, Bologna, Italy
3. National Center for Atmospheric Research, Boulder, CO, USA
4. Georgia Institute of Technology, Atlanta, GA, USA

Contents of this file

TABLE S1

ENSO				IOD			
Neg.		Pos.		Neg.		Pos.	
M07	1SD	M07	1SD	M07	1SD	M07	1SD
1916	1916	1911	1911	1915		1913	
1917	1917	1914	1914	1916	1916	1919	
1922	1922	1918	1918	1917	1917	1923	1923
1924	1924	1925		1930			1925
1928		1930	1930	1933		1926	
1933	1933	1940	1940		1941	1935	1935
1938	1938	1941	1941	1942	1942	1944	
1942	1942		1951	1958	1958	1945	1945
	1946	1957	1957		1960	1946	1946
	1948	1963	1963	1968			1949
1949		1965	1965	1974		1957	
1950		1972	1972	1975		1961	1961
1954	1954	1982	1982	1980		1963	1963
1955	1955	1986			1981		1967
1956		1987	1987	1985			1972
1964	1964	1991	1991	1989	1989		1976
1970		1997	1997		1990		1978
	1971		2002	1992	1992	1982	
1973	1973				1996		1986
1975	1975				1998	1991	
1978					2001	1994	1994
1981					2005	1997	1997
1984						1999	
1988	1988					2004	
1996							2006
1998	1998						
1999	1999						
2000							
	2007						

Table S1. ENSO and IOD years as classified by Meyers et al., 2007 (M07), and by using one standard deviation(1SD) threshold for JJASO mean values of N34 index and DMI.

FIG. S1

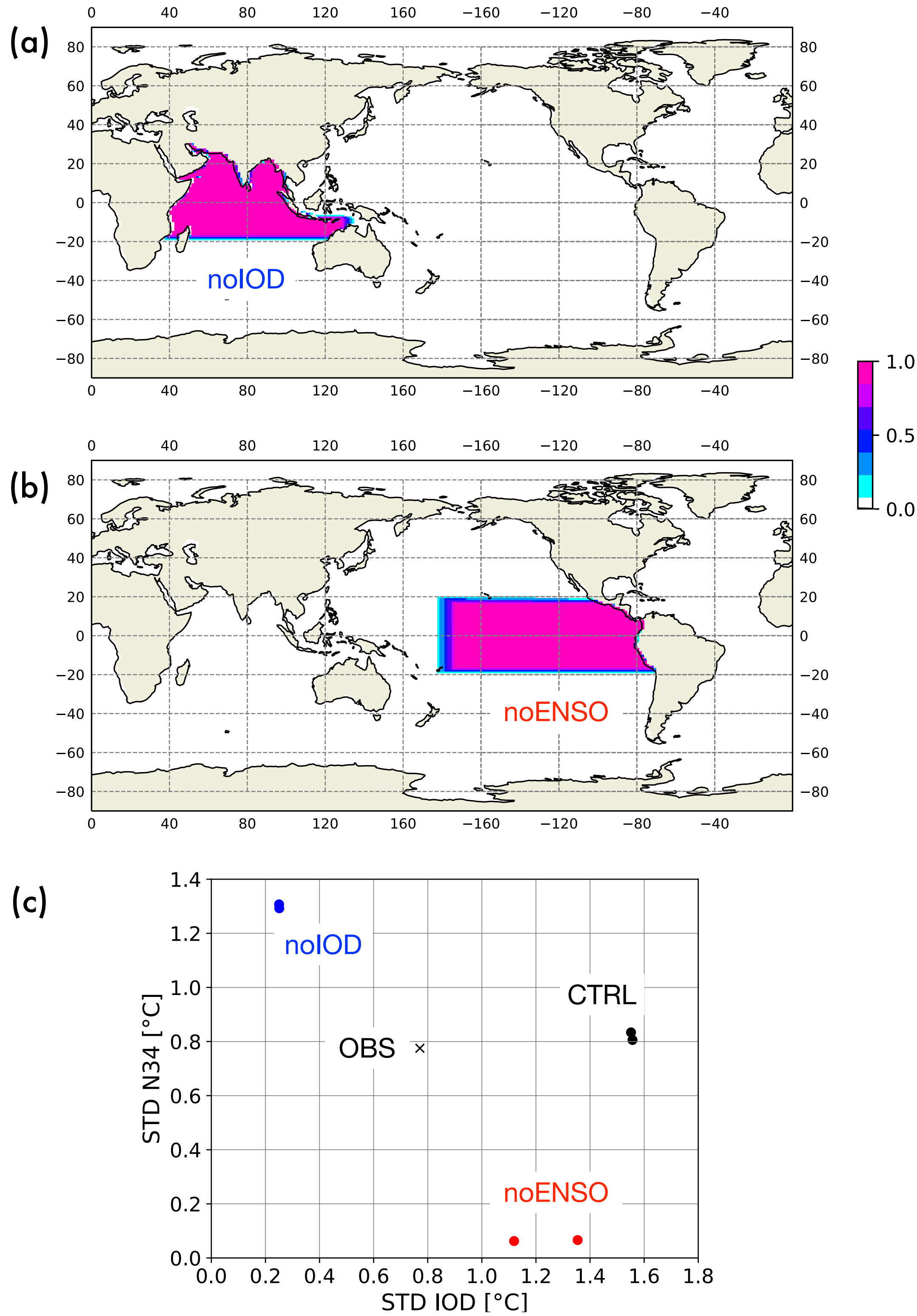

Fig. S1. Mask used for the partially-coupled experiments: noENSO-coupled (a) and noIOD-coupled (b). To avoid abrupt changes in the SST field, a buffer zone, in which the climatology combines linearly with model values, is used within 3° of the fully-restored region. The color shading indicates the values of the coefficient used to combine the two fields: 0 for modelled-only SST; and 1 for climatology-only SST. The lowest panel (c) shows the standard deviation (STD) of the monthly mean Niño3.4 and DMI index in the observation (ERSSTv5 from 1950-2018; black cross), the control (CTRL; black dots), and the noIOD-coupled (noIOD; blue dots), and the noENSO-coupled (noENSO; red dots) simulations. To partially assess the role of natural variability in these STD estimates, the 200-year long simulations have been analysed in two chunks of 100-years each, resulting in two points for each simulations.

FIG. S2

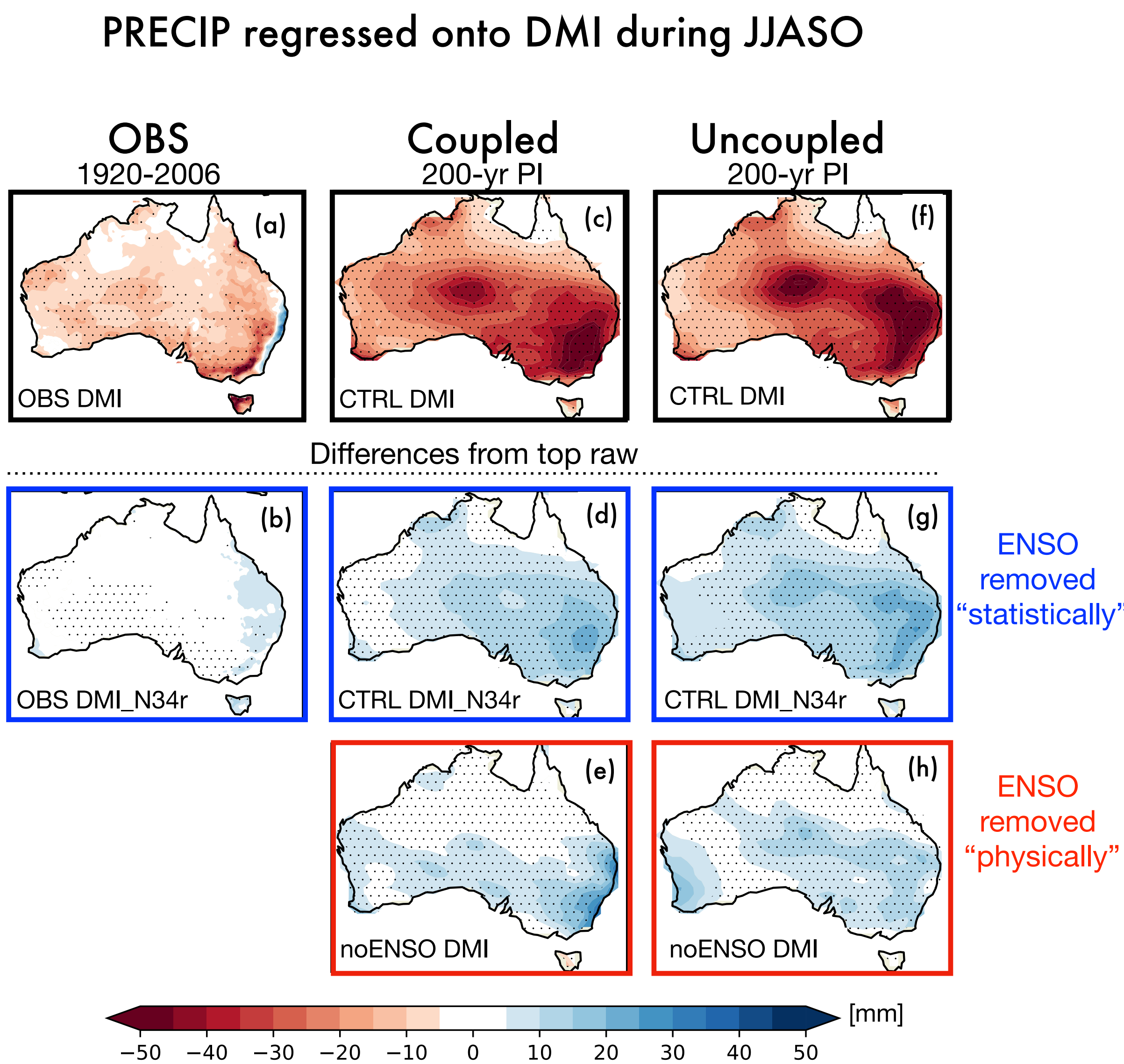

Fig. S2. Precipitation patterns associated with variability in DMI. Top raw: DMI index regressed onto mean rainfall anomaly (mm) in June-October for observation (a), the coupled (c) and the uncoupled (f) model simulations. Middle raw: as in the top raw but for rainfall anomalies in which the variability associated with the Niño3.4 index has been linearly removed. Results show differences with respect to the top raw for observation (b), coupled (c) and uncoupled (f) control simulations. Bottom raw: as in the top raw but for the simulations with removed ENSO variability, namely the noENSO-coupled (e) and the noENSO-uncoupled (h) simulations Results show differences with respect to the control simulation (top raw). The stippling over the maps indicates regions significant at 95% according to a two-tailed Student's t-test.

FIG. S3

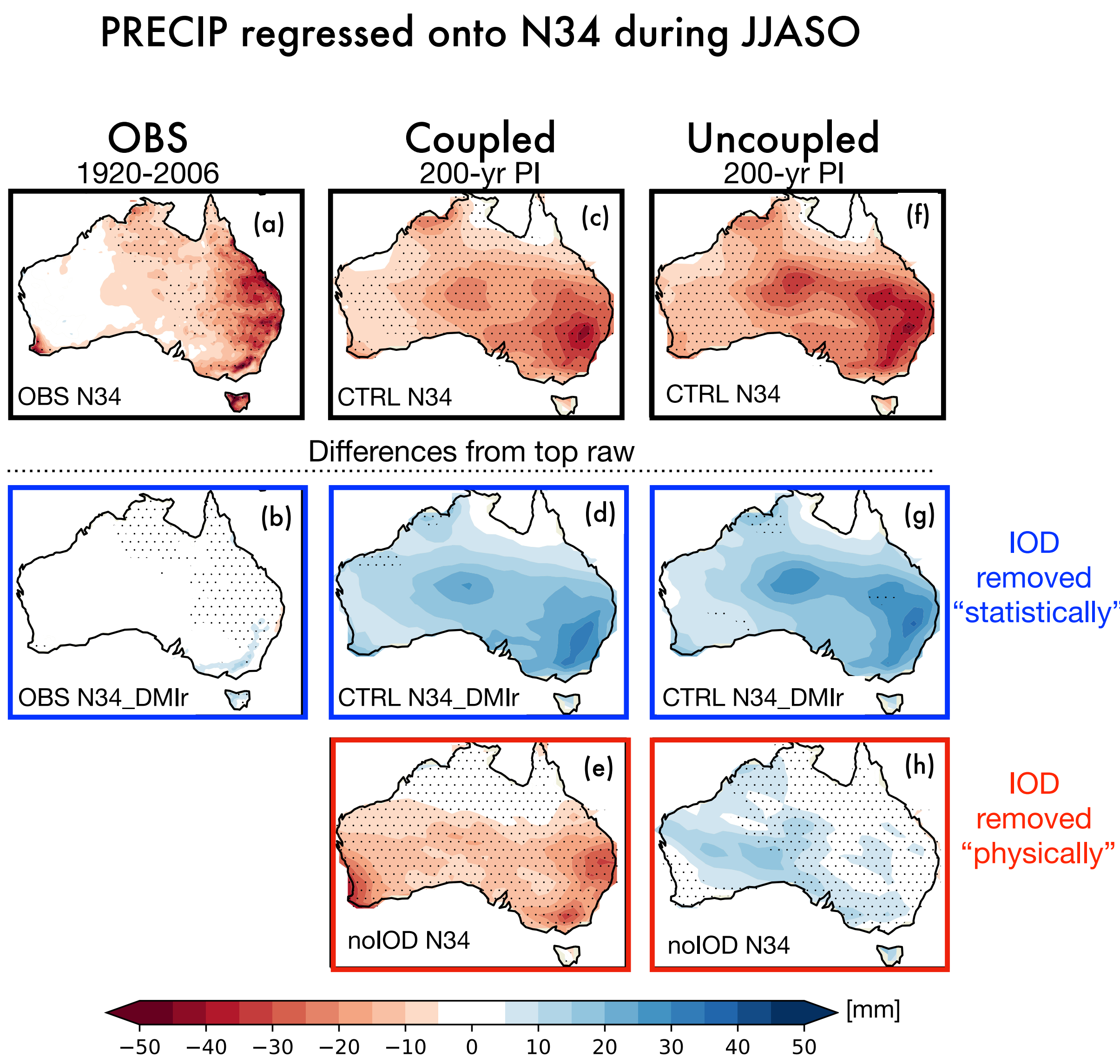

Fig. S3. Precipitation patterns associated with variability in DMI. Top raw: Niño3.4 index regressed onto mean rainfall anomaly (mm) in June-October for observation (a), the coupled (c) and the uncoupled (f) model simulations. Middle raw: as in the top raw but for rainfall anomalies in which the variability associated with the DMI index has been linearly removed. Results show differences with respect to the top raw for observation (b), coupled (c) and uncoupled (f) control simulations. Bottom raw: as in the top raw but for the simulations with removed IOD variability, namely the noIOD-coupled (e) and the noIOD-uncoupled (h) simulations Results show differences with respect to the control simulation (top raw). The stippling over the maps indicates regions significant at 95% according to a two-tailed Student's t-test.

FIG. S4

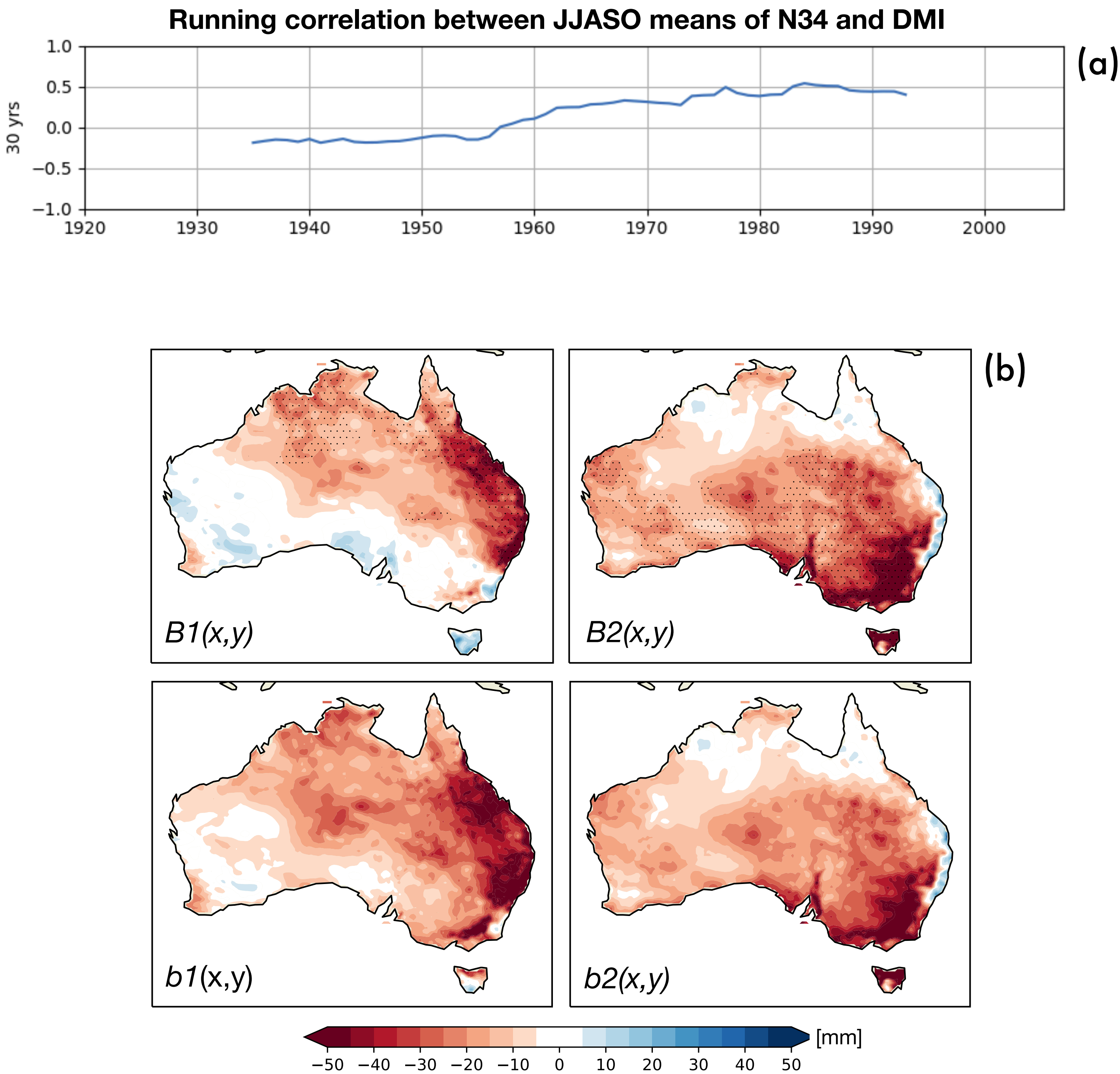

Fig. S4. (a) 30-year running correlation between N34 index and DMI from 1920 to 2007. (b) as in Figure 4a-d but for the latest 30 year period of available observations (1990-2019). The stippling over the maps indicates regions significant at 95% according to a two-tailed Student's t-test.

FIG. S5

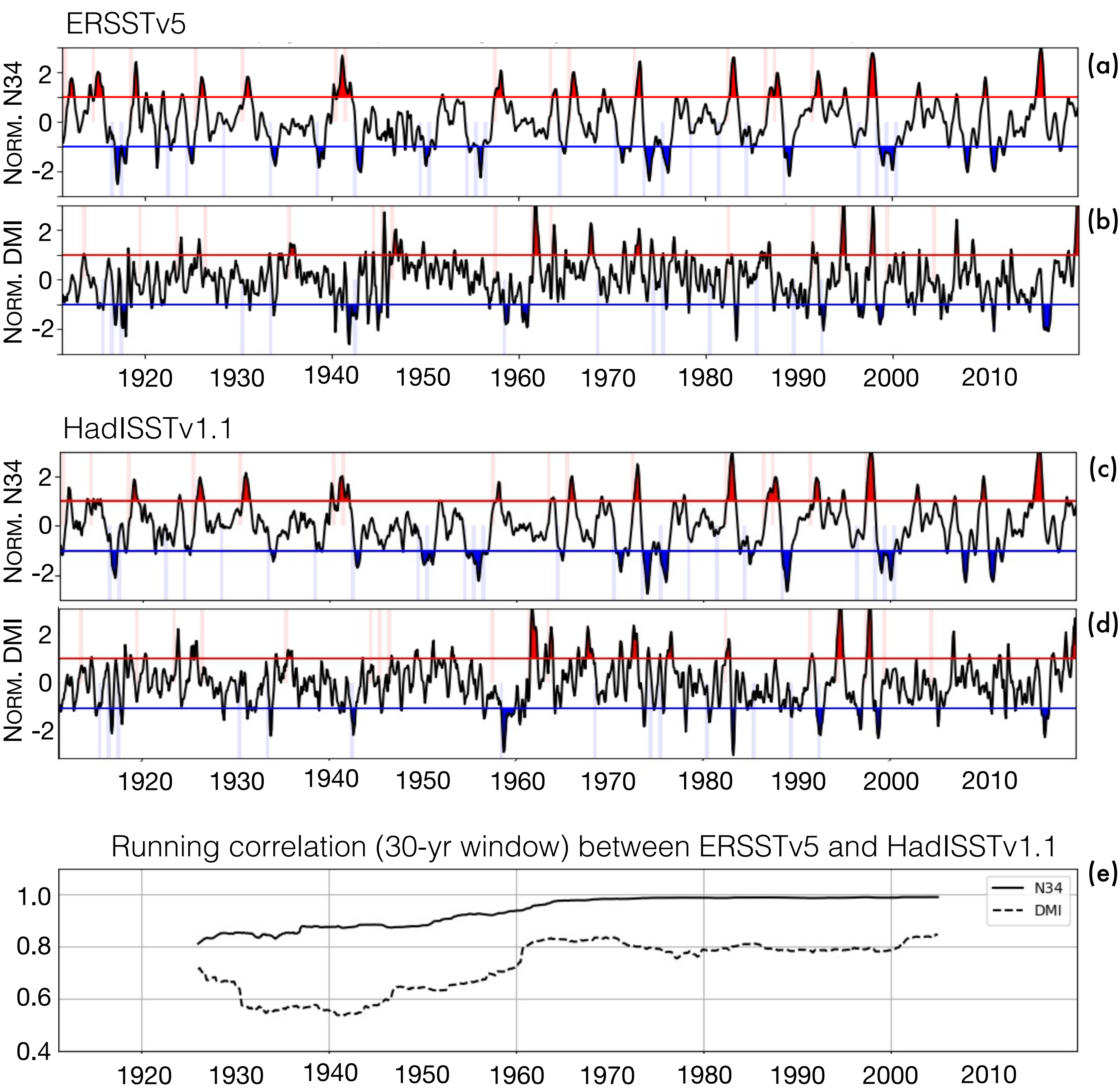

Fig. S5. ENSO/IOD index: datasets comparison . (a) Normalized time series of Niño3.4 index from 1911 to 2019 for vv dataset. The area of above (below) 1 standard deviation (STD) is filled in Red (blue) and the vertical red (blue) bars superimposed indicate years classified as positive (negative) ENSO by Meyers et al., 2007 (M07). (b) As in (a) but for DMI time series and IOD events. (c) and (d) repeat the analysis in (a) and (b) but using HadISSTv1.1 dataset. (e) Running correlation (30-yr window) for indices derived from ERSSTv5 and HadISSTv1.1 datasets.

FIG. S6

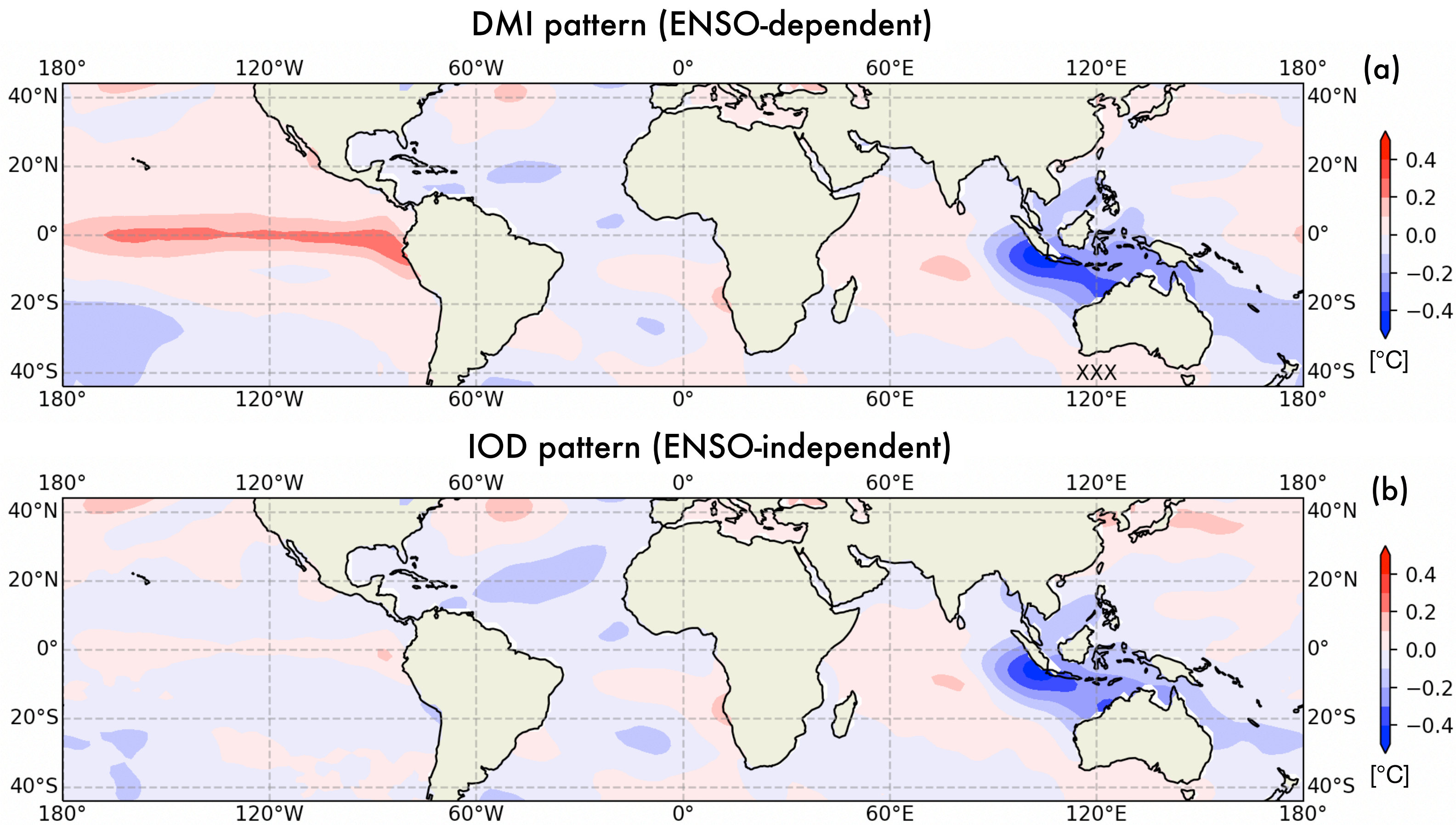

Fig. S6. (a) DMI index regressed onto sea surface temperature (°C) in June-October in the observation (ERSSTv5). (b) as in (a) but for the IOD index, which is defined as the DMI index minus the contribution associated (see equation 2b).

FIG. S7

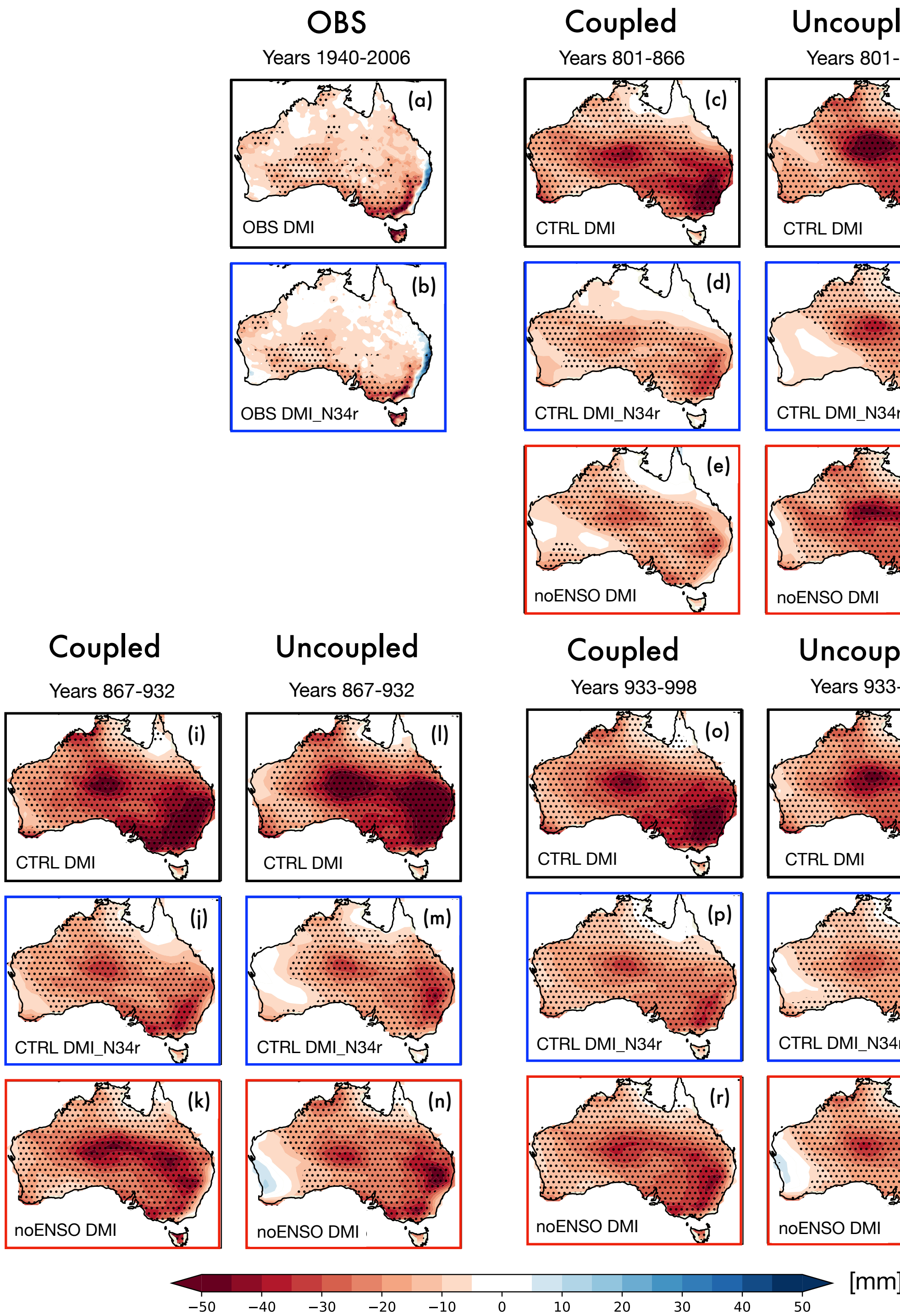

Fig. S7. Precipitation patterns associated with variability in DMI. Same as Fig. 2 except for the choice of the model years analysed. To explore low-frequency modulation in the teleconnections we divided the simulated period (200 years) in three chunks of 66 years. Top raws: DMI index regressed onto mean rainfall anomaly (mm) in June-October for observation (a), the coupled (c, i, and o) and the uncoupled (f, l, and s) model simulations. Middle raws: as in top raws but for rainfall anomalies in which the variability associated with the Niño3.4 index has been linearly removed. Results for observation (b), coupled (d, j, and p) and uncoupled (g, m, and t) control simulations. Bottom raws: as in top raws but for the simulations with removed ENSO variability, namely the noENSO-coupled (e, k, and r) and the noENSO-uncoupled (h, n, and u) simulations. All the experiments use pre-industrastrial (PI) condition for external forcing. The stippling over the maps indicates regions significant at 95% according to a two-tailed Student's t-test.

FIG. S8

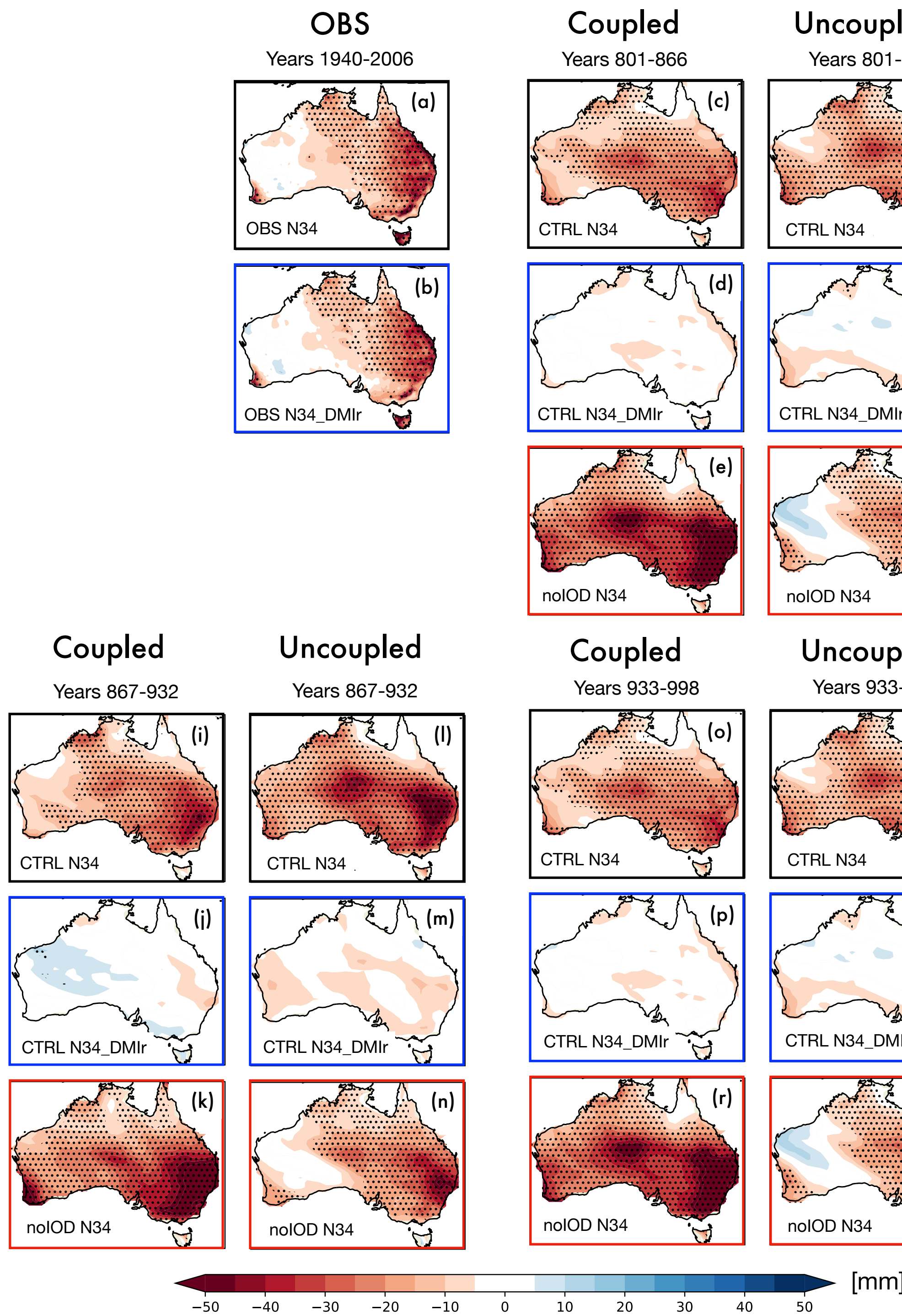

Fig. S8. Precipitation patterns associated with variability in Niño3.4. Same as Fig. 3 except for the choice of the model years analysed. To explore low-frequency modulation in the teleconnections we divided the simulated period (200 years) in three chunks of 66 years. Top raws: DMI index regressed onto mean rainfall anomaly (mm) in June-October for observation (a), the coupled (c, i, and o) and the uncoupled (f, l, and s) model simulations. Middle raws: as in top raws but for rainfall anomalies in which the variability associated with the DMI index has been linearly removed. Results for observation (b), coupled (d, j, and p) and uncoupled (g, m, and t) control simulations. Bottom raws: as in top raws but for the simulations with removed IOD variability, namely the noIOD-coupled (e, k, and r) and the noIOD-uncoupled (h, n, and u) simulations. All the experiments use pre-industrastrial (PI) condition for external forcing. The stippling over the maps indicates regions significant at 95% according to a two-tailed Student's t-test.